The Astrophysical Journal, 985:107 (14pp), 2025 May 20 https://doi.org/10.3847/1538-4357/adc57f

Possibility of Using 3.3 μm Polycyclic Aromatic Hydrocarbon Luminosity as a Molecular Gas Mass Estimator

Hyunjin Shim[1], Junhyun Baek[2], Dohyeong Kim[3], Minjin Kim[4], Hyunmi Song[5], Gu Lim[3,6], Jaejun Cho[4], Hayeong Jeong[3], Yejin Jeong[1], Ye-eun Kang[4], Dongseob Lee[1], Junyeong Park[3], Eunsuk Seo[5], Junho Song[5], and Been Yeo[2,7]
[1] Department of Earth Science Education, Kyungpook National University, Daegu 41566, Republic of Korea; hjshim@knu.ac.kr
[2] Korea Astronomy and Space Science Institute, Daejeon 34055, Republic of Korea
[3] Department of Earth Sciences, Pusan National University, Busan 46241, Republic of Korea
[4] Department of Astronomy and Atmospheric Sciences, Kyungpook National University, Daegu 41566, Republic of Korea
[5] Department of Astronomy and Space Science, Chungnam National University, Daejeon 34134, Republic of Korea
[6] Institute for Future Earth (IFE), Pusan National University, Busan 46241, Republic of Korea
[7] University of Science and Technology, Daejeon 34113, Republic of Korea
Received 2024 August 24; revised 2025 March 11; accepted 2025 March 24; published 2025 May 16

Abstract

We present CO(1–0) observations of 50 star-forming galaxies at $0.01 < z < 0.35$, for which 3.3 μm polycyclic aromatic hydrocarbon (PAH) emission flux or its upper limit is available. A scaling relation between 3.3 μm PAH luminosity and CO(1–0) luminosity is established covering ∼2 orders of magnitude in total IR luminosity and CO luminosity, with a scatter of ∼0.23 dex: $\log L_{3.3}/L_{\odot} = (1.00 \pm 0.07) \times \log L'_{\rm CO(1-0)}/({\rm K\ km\ s^{-1}\ pc^2}) + (-1.10 \pm 0.70)$. The slope is near unity, allowing the use of a single value of $\langle \log (L_{3.3}/L'_{\rm CO(1-0)}) \rangle = -1.09 \pm 0.36$ $[L_{\odot}/({\rm K\ km\ s^{-1}\ pc^2})]$ in the conversion between 3.3 μm PAH and CO luminosities. The variation in the $L_{3.3}/L'_{\rm CO}$ ratio is not dependent on the galaxy properties, including total IR luminosity, stellar mass, and star formation rate excess. The total gas mass, estimated using the dust-to-gas ratio and dust mass, is correlated with 3.3 μm PAH luminosity, in line with the prescription using $\alpha_{\rm CO} = 0.8$–4.5 covering both normal star-forming galaxies and starburst galaxies. Active galactic nucleus (AGN)-dominated galaxies tend to have a lower $L_{3.3}/L'_{\rm CO}$ than non-AGN galaxies, which needs to be investigated further with an increased sample size. The established $L_{3.3}$–$L'_{\rm CO}$ correlation is expected to be applicable to wide-field near-infrared spectrophotometric surveys that allow the detection of 3.3 μm emission from numerous low-redshift galaxies.

Unified Astronomy Thesaurus concepts: Luminous infrared galaxies (946); Ultraluminous infrared galaxies (1735); Starburst galaxies (1570); Polycyclic aromatic hydrocarbons (1280); Molecular gas (1073); Star formation (1569); Galaxies (573)

1. Introduction

Star formation is one of the most important processes in galaxy formation, evolution, and growth. An overall history of cosmic star formation, which has been continuously declining since $z \sim 2$ (P. Madau & M. Dickinson 2014), is consistent with the history of global stellar mass density while the stellar mass is described as an integration of the past star formation rate (SFR). Observed scaling relations between stellar mass, SFR, and gas-phase metallicity (e.g., C. A. Tremonti et al. 2004; F. Mannucci et al. 2010; S. Wuyts et al. 2011; J. S. Speagle et al. 2014) suggest relatively tight correlations between these parameters, implying that the star formation is regulated by molecular gas, which is a fuel to star formation, while a universal equilibrium exists between physical processes including gas supply, star formation, and gas expulsions as well as recycling (N. Bouché et al. 2010; S. J. Lilly et al. 2013).

Based on the well-known tight correlations between SFR and gas surface density for star-forming galaxies (M. Schmidt 1959; R. C. Kennicutt 1998), the decline of global SFR density could result from the decrease of gas content in galaxies (P. S. Behroozi et al. 2013), while the gas mass fraction in high-redshift star-forming galaxies is observed to be higher than that in local spiral galaxies (E. Daddi et al. 2010; L. J. Tacconi et al. 2010; A. Saintonge et al. 2011). The amount of young stars formed per unit of the molecular gas mass ($\equiv {\rm SFR}/M_{\rm gas}$), defined as a star formation efficiency, is known to be elevated in starburst galaxies (P. M. Solomon et al. 1997; R. Genzel et al. 2010; S. García-Burillo et al. 2012). While star formation in galaxies could be classified into two different modes, one for normal main-sequence mode and the other for starburst mode (D. Elbaz et al. 2011), the star formation efficiency may vary locally within galaxies, due to the varying giant molecular cloud formation in different interstellar medium environments (A. K. Leroy et al. 2008). To get a full understanding of the characteristics of star-forming galaxy populations at different epochs and to trace their evolution history, it is necessary to study the star formation efficiency through the measurement of SFR as well as the estimates of the molecular gas mass.

Due to the nonpolar nature of the hydrogen molecule (H_2), molecular gas in galaxies is in general traced using indirect tracers, one of the most commonly employed being the rotational transition line of the carbon monoxide (CO; e.g., J. S. Young & N. Z. Scoville 1991; J. S. Young et al. 1995; A. Saintonge et al. 2011; M. S. Bothwell et al. 2013). The observed CO luminosity is converted to H_2 mass using the CO-to-H_2 conversion factor ($\alpha_{\rm CO}$), which is known to vary for galaxies with different physical parameters such as SFR, metallicity, and gas dynamics (A. K. Leroy et al. 2011; A. D. Bolatto et al. 2013). To reduce uncertainties in molecular gas estimates due to $\alpha_{\rm CO}$ uncertainties and to complement gas estimates that require CO line detection, other strategies have

been suggested including the use of far-infrared (FIR) fluxes in estimating the dust mass and scaling it to the gas mass by applying the dust-to-gas ratio (N. Scoville et al. 2014, 2016; S. Berta et al. 2016), which also has inherent uncertainties due to dust modeling uncertainty and the metallicity dependence of the dust-to-gas ratio (A. Rémy-Ruyer et al. 2014).

Recently, I. Cortzen et al. (2019) suggested that there exists a universal scaling relation between mid-infrared (MIR; 6.2 and 7.7 μm) polycyclic aromatic hydrocarbon (PAH) luminosity and CO luminosity for star-forming galaxies. PAH molecules in the photodissociation regions, excited by the far-ultraviolet stellar radiation, produce strong emission features at 3.3, 6.2, 7.7, 8.6, 11.3, and 12.7 μm. Therefore, PAH emission has been suggested to be a qualitative and quantitative tracer of star formation in a wide range of galaxies (E. Peeters et al. 2004; H. V. Shipley et al. 2016). Considering the tight correlation between SFR and molecular gas mass, it is naturally expected that PAH emission and molecular gas content would show a correlation. The correlation between PAH and CO emission is being investigated even in spatially resolved scales for nearby galaxies (J. Chastenet et al. 2023; A. K. Leroy et al. 2023 ; R. Chown et al. 2025).

While the shortest wavelength PAH emission feature, i.e., 3.3 μm PAH emission, is much weaker in terms of the flux density thus less investigated so far compared to longer PAH emission features, the potential of using 3.3 μm PAH in the study of star formation in nearby galaxies (through all-sky near-infrared, hereafter NIR, spectrophotometric surveys such as SPHEREx; O. Doré et al. 2018) is promising due to the large sample size. Since the 3.3 μm PAH is the shortest among PAH features, it serves as a tracer of dust-free star formation in star-forming galaxies at the reionization era (using MIR spectroscopic instruments such as JWST MIRI). To use 3.3 μm PAH emission either in SFR estimation or in the molecular gas mass estimation, an assessment of whether there exists a correlation between 3.3 μm PAH and CO luminosities should be preceded using samples with both PAH and CO observations.

In this work, we establish the scaling relation between the 3.3 μm PAH luminosity and gas content (CO luminosity and molecular gas mass) using new single-dish (SD) CO(1–0) observations of 50 objects including both star-forming galaxies and active galactic nucleus (AGN). The sources, i.e., targets of new CO observations, are selected from literature listing 3.3 μm PAH flux measurements (Section 2.1). By adding measurements from our new observations (Sections 2.2 and 2.3) to the existing data (Section 2.4), the number of objects for which both 3.3 μm and CO luminosities are available has increased by a factor of $\sim$1.6. We present the constructed $L_{3.3}$–$L'_{\rm CO}$ correlation in Section 3.1 and discuss the molecular gas mass estimation from 3.3 μm PAH in Section 3.2. In addition to the overall $L_{3.3}$–$L'_{\rm CO}$ correlation, a comparison between AGN-dominated galaxies and non-AGN galaxies is investigated in Section 3.3. Throughout the paper, we use the flat ΛCDM cosmology model with $\Omega_{\rm m,0} = 0.3$, $H_0 = 70\,{\rm km\,s^{-1}\,Mpc^{-1}}$. When using values from different literature, the differences in cosmological parameters are taken into account.

2. Data

2.1. 3.3 μm PAH-selected Galaxies

To explore the relationship between 3.3 μm PAH luminosity and CO luminosity, we constructed a 3.3 μm PAH-selected sample of 180 sources at $0.01 < z < 0.35$ by compiling the previous 2.5–5 μm spectroscopic observations from the infrared satellite AKARI (R. Yamada et al. 2013; J. H. Kim et al. 2019; T. S. Y. Lai et al. 2020). The 2.5–5 μm spectra were obtained with the Infrared Camera (IRC; T. Onaka et al. 2007), utilizing the near-infrared grism mode for point-source spectroscopy that yields the spectroscopic resolution of $R \sim 120$ (Y. Ohyama et al. 2007). The observations were made with a $1' \times 1'$ aperture; thus, the 3.3 μm PAH luminosity measured from the AKARI/IRC spectrum corresponds to the value integrated over the entire galaxy if the galaxy is smaller than $1'$. The target selection varied across different IRC programs, including MIR excess sources with higher 9 μm flux density compared to the K_s-band flux density (S. Oyabu et al. 2011), local luminous infrared galaxies (LIRGs; $\log(L_{\rm IR}/L_\odot) > 11$) and ultraluminous infrared galaxies (ULIRGs; $\log(L_{\rm IR}/L_\odot) > 12$) (M. Imanishi et al. 2008, 2010), and unusual galaxies such as low-metallicity dwarf galaxies (T. S. Y. Lai et al. 2020). Therefore, the 3.3 μm PAH-selected sample consists of heterogeneous galaxy populations, covering a wide range of total infrared luminosities ($10^{9-12.5}\,L_\odot$), including both AGN-dominated and star formation-dominated systems.

For the sources from T. S. Y. Lai et al. (2020), the luminosities of PAH emission features at other wavelengths (e.g., 6.2, 7.7, and 11.3 μm) are also available since the sources are from the constructed list of "bright-PAH" galaxies, which have spectra with full coverage from 2.5 to 38 μm by combining the Spitzer (IDEOS; A. Hernán-Caballero et al. 2016; H. W. W. Spoon et al. 2022) and AKARI spectra. To include the AKARI sources that are not matched to the IDEOS catalog, we used the works by R. Yamada et al. (2013) and J. H. Kim et al. (2019). Note that the data reduction package versions are different for different works, e.g., "IRC Spectroscopy Toolkit for Phase 3 data Version 20090211" (R. Yamada et al. 2013) and "IRC Spectroscopy Toolkit for Phase 3 data Version 20170225" (T. S. Y. Lai et al. 2020) for Phase 3 data, "IRC Spectroscopy Toolkit Version 20090211" (R. Yamada et al. 2013) and "IRC Spectroscopy Toolkit Version 20080528" (T. S. Y. Lai et al. 2020) for Phases 1 and 2 data. The major updates on the data reduction package were related to the revision of the wavelength and spectral response calibrations of grism[8]; thus, the 3.3 μm PAH luminosity values of a single source presented in multiple works differ from each other due to flux calibration uncertainties and different aperture sizes used in spectra extraction. In addition to these, different works used different treatments for dust attenuation correction. T. S. Y. Lai et al. (2020) present attenuation-corrected 3.3 μm PAH luminosity based on the two different dust geometry assumptions, mixed and obscured continuum. The 3.3 μm PAH luminosity values presented by R. Yamada et al. (2013) and J. H. Kim et al. (2019) are not corrected for dust attenuation.

The numbers of sources compiled from T. S. Y. Lai et al. (2020), R. Yamada et al. (2013), and J. H. Kim et al. (2019) are 112, 95, and 14, respectively. For 41 sources from T. S. Y. Lai et al. (2020) that overlap with sources in R. Yamada et al. (2013), the average difference in $\log L_{3.3}$ values is 0.055 ± 0.145 and 0.237 ± 0.198 dex when obscured continuum and mixed geometry assumptions were used, respectively. In the case of the 3.3 μm PAH luminosity values corrected for mixed dust geometry, $\Delta \log L_{3.3}$ (discrepancy from the value without attenuation correction) tends to correlate with the 3.3 μm PAH

[8] https://www.ir.isas.jaxa.jp/AKARI/Observation/support/IRC/

luminosity. Therefore, to reduce the uncertainties generated by the systematic difference between different log $L_{3.3}$ values, we used 3.3 μm PAH luminosity corrected for dust attenuation based on the obscured continuum geometry, rather than the mixed geometry, for 112 sources from T. S. Y. Lai et al. (2020). Among 54 additional sources from R. Yamada et al. (2013), 18 sources are not detected in 3.3 μm, as well as 12 out of 14 sources in J. H. Kim et al. (2019). For these, 3.3 μm upper limits were compiled.

The multiwavelength photometry data points covering UV, optical, NIR, MIR, and FIR regimes were compiled for 3.3 μm PAH-selected sources by cross-identifying the positions of sources in the archival Galaxy Evolution Explorer (GALEX; L. Bianchi et al. 2017), SDSS (S. Alam et al. 2015), Two Micron All Sky Survey (2MASS; M. F. Skrutskie et al. 2006), UKIRT Infrared Deep Sky Survey (UKIDSS; A. Lawrence et al. 2007), Wide-field Infrared Survey Explorer (WISE; E. L. Wright et al. 2010), IRAS (M. Moshir et al. 1992), AKARI (I. Yamamura et al. 2010), and Herschel/SPIRE (Herschel Team et al. 2024) source catalogs. The search radius was 3″ in optical and 6″ in other wavelengths, and the total (integrated) flux density was adopted when the source was spatially resolved.

Using the photometry compilation, the physical properties of each source including stellar mass, SFR, and dust mass were derived through spectral energy distribution (SED) fitting. The SED fitting was performed using CIGALE[9] (Code Investigating GALaxy Emission; S. Noll et al. 2009; M. Boquien et al. 2019), with similar configurations as in H. Shim et al. (2023). The `bc03` (G. Bruzual & S. Charlot 2003) stellar population model with the delayed star formation history (`sfhdelayed`) was used to estimate stellar mass and SFR. The MIR to FIR SED was fitted using the `dl2014` (B. T. Draine et al. 2014) dust emission model with varying PAH mass fraction, stellar radiation field intensity, and the fraction of the dust mass exposed to starlight. While the AGN component contribution to the SED is also estimated using `fritz2006` model (J. Fritz et al. 2006), we did not use the AGN fraction in the type classification among 3.3 μm PAH-selected sources since the AGN classification based on the SED fitting requires fine sampling of the MIR SED (e.g., T.-W. Wang et al. 2020). Instead, we used either optical spectra (from SDSS) or MIR colors (from WISE) to classify sources into AGN-dominated and star formation-dominated subgroups, based on the existence of broad lines and/or (W1 − W2) versus (W2 − W3) colors (using the criteria of S. Mateos et al. 2012) that reflect the warm dusty torus (T. H. Jarrett et al. 2011; S. Mateos et al. 2012).

Figure 1 shows the total IR luminosity (integrated over 8–1000 μm), SFR, and stellar mass distributions of the 3.3 μm PAH-selected sources. Most (over 70%) sources are classified as either LIRGs or ULIRGs, corresponding to an SFR of 10–1000 $M_\odot$ yr^{-1}. In the SFR–stellar mass diagram, these galaxies are located on average ∼1 dex above the main sequence of star-forming galaxies at $z < 0.3$ (J. S. Speagle et al. 2014; P. Popesso et al. 2023).

Previous works have discussed that prominent MIR (e.g., 6.2 and 7.7 μm) PAH features get weakened as the IR luminosity increases, with the typical L(PAH)–L(IR) relation breaking at around log $(L_{IR}/L_\odot) \sim 11.5$ for local galaxies

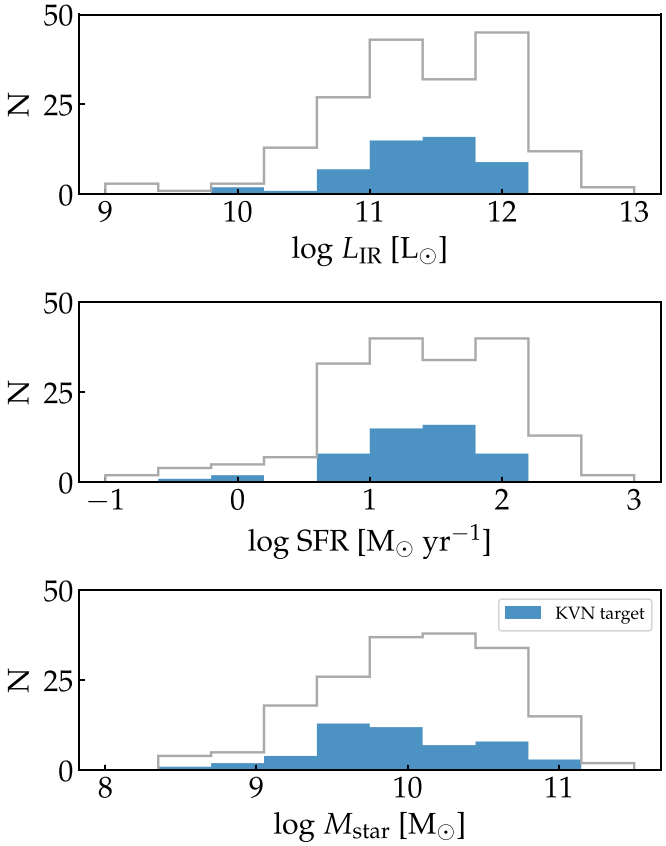

Figure 1. Total infrared luminosity (top), star formation rate (middle), and stellar mass (bottom) distributions of the 3.3 μm selected sources. Shaded histograms correspond to 50 targets in our KVN CO observation programs.

(I. Cortzen et al. 2019) and log $(L_{IR}/L_\odot) \sim 12.5$ for higher-redshift galaxies (A. Pope et al. 2008, 2013; H. V. Shipley et al. 2016). In the case of 3.3 μm PAH, T. S. Y. Lai et al. (2020) showed that the luminosity ratio $L_{3.3}/L_{IR}$ is nearly constant at below log $(L_{IR}/L_\odot) = 11.2$. Figure 2 shows the correlation between total IR luminosity and 3.3 μm PAH luminosity. The best-fit linear correlation between log $L_{3.3}$ and log L_{IR} (black solid line in Figure 2) is derived using the approach described in B. C. Kelly (2007), and is expressed as

$$\log L_{3.3} = (0.80 \pm 0.04) \times \log L_{IR} + (-0.85 \pm 0.51). \quad (1)$$

By excluding points with $L_{3.3}$ upper limits, i.e., censoring these points, the derived relationship (brown solid line in Figure 2) is comparable to the original one within an intrinsic scatter ($\sigma \sim 0.36$ dex). The subunity (0.80) slope between log $L_{3.3}$ and log L_{IR} is comparable to that of the cases of log $L_{6.2}$ and log $L_{7.7}$ (I. Cortzen et al. 2019). The derived trend remains almost the same if AGN are excluded; note that it cannot be ruled out as such that no change is due to the small number of AGN compared to non-AGN. The main reason causing a subunity slope is the decrease of log $(L_{3.3}/L_{IR})$ at log $(L_{IR}/L_\odot) > 11.2$; the median of the $(L_{3.3}/L_{IR})$ decreases as the IR luminosity increases, consistent with the findings of T. S. Y. Lai et al. (2020; using $L_{3.3}$ corrected for dust attenuation assuming obscured continuum geometry).

2.2. New CO(1–0) Observations

The Korean Very Long Baseline Interferometry Network (KVN) is a long baseline interferometry network in Korea that

[9] https://cigale.lam.fr/2020/06/29/version-2020-0/

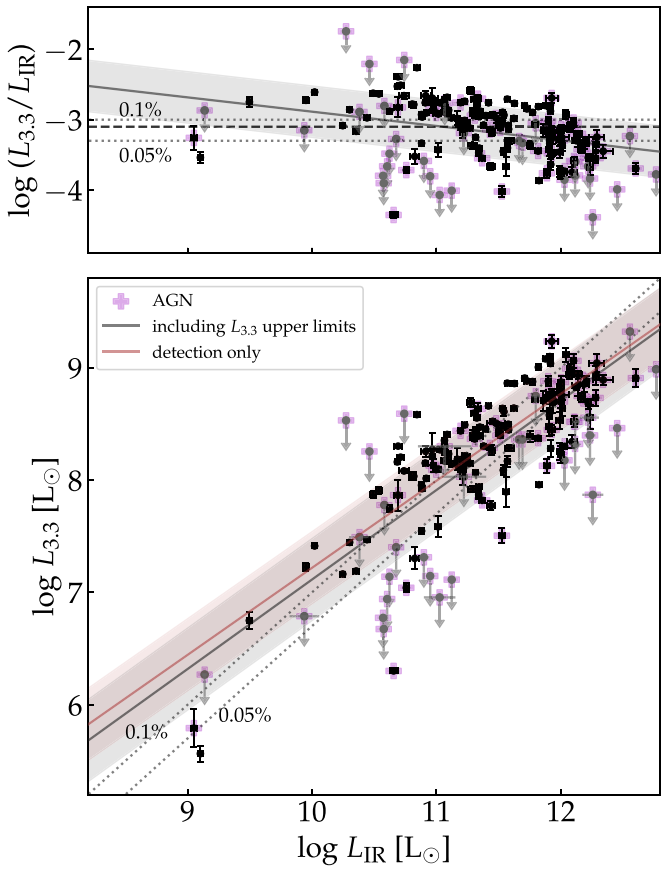

Figure 2. Comparison between 3.3 μm PAH luminosity and total IR luminosity. Potential AGN, identified by either broad hydrogen recombination lines or MIR colors, are marked with crosses. Solid lines depict the best-fit linear relationship between the log $L_{3.3}$ vs. log L_{IR}, while shaded regions represent the intrinsic scatter of the fits. The dashed line in the upper panel is a horizontal line at −3.1, corresponding to the mean log ($L_{3.3}/L_{IR}$) value for the entire sample (150 sources, excluding 30 sources with 3.3 μm upper limits). Dotted lines represent $L_{3.3}/L_{IR}$ = 0.1% and 0.05%, a typical range of 3.3 μm PAH luminosity (R. Yamada et al. 2013; T. S. Y. Lai et al. 2020).

consists of three 21 m radio antennas located at Yonsei (KYS), Ulsan (KUS), and Tamna (KTN) sites (S.-S. Lee et al. 2011), with a fourth site added in mid-2024 at Pyeongchang. Besides its capability for performing interferometry observations, the KVN also offers the SD observing mode.

We carried out CO(1–0) observations of 50 3.3 μm PAH-selected galaxies (Table 1) using the three antennas with the SD observing mode, from 2023 December to 2024 March. The targets for the KVN observations were selected based on their visibility. The beam size (half power beamwidth) of the KVN 21 m antennas at ∼115 GHz is ∼30″, so we prioritized sources with optical radii (D_{25}) smaller than 60″, twice the beam size. However, due to the proximity of the sources where 3.3 μm PAHs are available, ∼30% of the KVN sources (16 out of 50) have optical radii larger than 60″, raising the possibility that their CO measurements could be a lower limit. The IR luminosity and SFR distribution of the KVN targets are similar to those of the parent 3.3 μm sample (Figure 1), while the stellar masses of the KVN targets are slightly lower as the smaller-sized sources were prioritized.

All sources were observed using the *W* band (80–116 GHz) with the central frequency of the GPU spectrometer tuned to the expected CO(1–0) frequency of each target and the backend (wide-field sampler, OCTAD) bandwidth of 1024 MHz. The observations were executed in a position-switching mode, i.e., consecutively having 10 s of off-source exposure after each 10 s of on-source exposure for proper removal of the sky background. The actual on-source integration time varies for different objects (between 0.5 and 4.5 hr), since we stopped the integration if the signal-to-noise ratio (S/N) > 5 was reached for the CO emission line with a spectral resolution of 10 km s^{-1}. During the observations, pointing calibrations were performed every ∼3 hr by observing position reference sources. Focus adjustments were made every ∼6 hr.

2.3. Data Reduction

Spectral data reduction was done using the IRAM GILDAS/CLASS[10] software (Gildas Team 2013). We inspected individual spectra for a given observing target to exclude low-quality scans, such as those with highly fluctuating baselines due to bad weather conditions. Then, the remaining scans were averaged using σ weighting, i.e., weighted by the inverse square of the rms noise of each individual spectrum. The rms noise was estimated in each individual spectrum by assuming a linear baseline outside a window of [−600, +600] km s^{-1}. The averaged spectra were smoothed to the velocity resolution of ∼10 km s^{-1}.

To convert the antenna temperature (T_A^*) in kelvins into the flux density Jy in the averaged spectra, we used the degree per flux density unit values described in the 2023 KVN status report[11] (0.0572, 0.0685, 0.0548 K Jy^{-1} for KYS, KUS, KTN site, respectively). The CO(1–0) line luminosities, L'_{CO}, were estimated in units of [K km s^{-1} pc^2] using the following equation (P. M. Solomon et al. 1997; P. M. Solomon & P. A. Vanden Bout 2005):

$$L'_{CO} = 3.25 \times 10^7 S_{CO}\Delta v\, \nu_{obs}^{-2}\, D_L^2 (1+z)^{-3}, \quad (2)$$

where $S_{CO}\Delta v$ is the velocity-integrated flux density in Jy km s^{-1}, ν_{obs} is the observed frequency in GHz, and D_L is the luminosity distance in Mpc.

Figure 3 shows the CO(1–0) spectra of the 50 targets in our KVN observation programs. The line is considered to be detected if the peak antenna temperature is above 4σ. We detected a CO(1–0) line for 44 (88%) out of 50 sources. Some sources clearly show a double-peaked line profile, which is often asymmetric, reflecting the rotational motion of the molecular gas. For sources where the CO line is approximated as a single Gaussian, we consider the FWHM of the Gaussian profile as the line width (ΔW). In the case of a double-peaked line profile, we assume the width of the double-horned shape to be the line width. The velocity-integrated CO flux density $S_{CO}\Delta v$ was derived by integrating the area under the line in the integration range of [−1.5 ΔW, +1.5 ΔW] from the line center. By changing the integration range to [−ΔW, +ΔW], the flux density decreases by 1%–9%, which is minimal compared to the scatter in CO measurements from different transitions and observing methods (Section 2.4, Figure 4).

The $S_{CO}\Delta v$, line width (FWHM; ΔW), and other observation-related properties such as the coordinate, redshift

[10] http://www.iram.fr/IRAMFR/GILDAS/
[11] https://radio.kasi.re.kr/status_report/files/KVN_status_report_2023.pdf

Table 1
Summary of the KVN SD CO(1–0) Observations of the 3.3 μm PAH-selected Galaxies

Name	R.A.	Decl.	z_{CO}	$S_{CO}\Delta v$	FWHM	log $L_{3.3}$	log $L'_{CO(1-0)}$	rms
	(hh:mm:ss)	(dd:mm:ss)		(Jy km s^{-1})	(km s^{-1})	($L_\odot$)	(K km s^{-1} pc^2)	(mK)
(1)	(2)	(3)	(4)	(5)	(6)	(7)	(8)	(9)
NGC 0023	00:09:53.41	+25:55:25.6	0.0153	113.3 ± 10.5	352	8.21 ± 0.01	9.08 ± 0.40	2.1
MCG+12-02-001[a]	00:54:03.61	+73:05:11.8	0.0162	69.1 ± 6.5	144	8.39 ± 0.01	8.89 ± 0.06	2.9
CGCG 436-030	01:20:02.72	+14:21:42.9	0.0313	39.4 ± 6.1	209	8.51 ± 0.02	9.24 ± 0.31	2.2
III Zw 035	01:44:30.50	+17:06:05.0	0.0275	40.7 ± 4.4	222	7.77 ± 0.04	9.15 ± 0.16	1.4
NGC 0695	01:51:14.24	+22:34:56.5	0.0324	86.5 ± 10.6	211	8.86 ± 0.01	9.62 ± 0.44	3.2
UGC 01385	01:54:53.79	+36:55:04.6	0.0185	58.6 ± 5.5	95	8.02 ± 0.02	8.97 ± 0.09	3.4
UGC 01845	02:24:07.98	+47:58:11.0	0.0147	117.2 ± 16.5	281	8.23 ± 0.02	9.11 ± 0.26	5.1
NGC 0992	02:37:25.49	+21:06:03.0	0.0136	83.0 ± 8.2	283	8.20 ± 0.01	8.85 ± 0.33	2.3
UGC 02238	02:46:17.49	+13:05:44.4	0.0219	107.8 ± 10.5	347	8.60 ± 0.01	9.37 ± 0.10	2.9
UGC 02369[a]	02:54:01.78	+14:58:25.0	0.0316	70.2 ± 10.1	255	8.46 ± 0.04	9.49 ± 0.16	2.5
SDSS J032322.86-075615.2	03:23:22.86	−07:56:15.3	0.1664[b]	<14.4	⋯	8.84 ± 0.09	<10.29	0.8
UGC 02982	04:12:22.45	+05:32:50.6	0.0178	122.2 ± 7.5	362	8.41 ± 0.01	9.20 ± 0.50	1.8
NGC 1614	04:33:59.85	−08:34:43.9	0.0159	103.2 ± 9.1	245	8.64 ± 0.01	9.07 ± 0.45	2.3
VII Zw 031	05:16:46.09	+79:40:13.2	0.0544	61.7 ± 7.9	169	9.08 ± 0.01	9.91 ± 0.49	2.8
NGC 2388	07:28:53.44	+33:49:08.7	0.0136	173.5 ± 9.6	253	8.12 ± 0.01	9.17 ± 0.15	2.2
2MASX J08310928+5533165	08:31:09.29	+55:33:16.4	0.0448	3.4 ± 0.9	51	7.58 ± 0.07	8.50 ± 0.26	1.2
NGC 2623	08:38:24.07	+25:45:16.7	0.0184	88.9 ± 9.2	268	7.82 ± 0.01	9.14 ± 0.28	1.9
UGC 04730	09:01:58.39	+60:09:06.1	0.0113	44.6 ± 7.7	735	7.41 ± 0.02	8.39 ± 0.25	1.0
2MASX J09024894+5236247	09:02:48.90	+52:36:24.6	0.1573	8.3 ± 2.0	333	8.86 ± 0.07	10.00 ± 0.26	0.5
UGC 04881[a]	09:15:55.10	+44:19:55.0	0.0399	65.6 ± 6.4	247	8.29 ± 0.03	9.67 ± 0.24	1.8
NGC 3110	10:04:02.11	−06:28:29.2	0.0169	157.0 ± 11.3	303	8.35 ± 0.01	9.31 ± 0.33	2.9
2MASX J10522356+4408474	10:52:23.52	+44:08:47.7	0.0921[b]	< 32.6	⋯	8.76 ± 0.04	<10.11	2.1
Arp 148[a]	11:03:53.20	+40:50:57.0	0.0348	85.8 ± 16.3	487	8.42 ± 0.03	9.67 ± 0.25	2.4
SBS 1133+572	11:35:49.07	+56:57:08.2	0.0517	19.6 ± 3.4	518	8.63 ± 0.05	9.37 ± 0.25	0.6
Mrk 1457	11:47:21.61	+52:26:58.5	0.0487	8.6 ± 1.6	126	8.13 ± 0.06	8.97 ± 0.25	0.8
IC 0836	12:55:54.02	+63:36:44.4	0.0093	17.9 ± 4.1	360	7.23 ± 0.04	7.84 ± 0.26	1.6
VV 283a	13:01:50.26	+04:20:01.9	0.0375	83.7 ± 12.7	359	8.49 ± 0.02	9.73 ± 0.09	2.7
IC 0860	13:15:03.52	+24:37:07.9	0.0130	50.0 ± 3.6	183	7.04 ± 0.04	8.57 ± 0.24	1.2
UGC 08335[a]	13:15:32.80	+62:07:37.0	0.0315	21.5 ± 3.2	275	8.61 ± 0.04	8.95 ± 0.25	0.9
NGC 5104	13:21:23.09	+00:20:32.6	0.0185	135.7 ± 17.1	488	8.209 ± 0.02	9.33 ± 0.06	2.7
NGC 5256[a]	13:38:17.50	+48:16:37.0	0.0283	51.0 ± 5.1	343	8.37 ± 0.02	9.25 ± 0.62	1.0
2MASX J13561001+2905355	13:56:10.00	+29:05:35.2	0.1089	23.1 ± 4.0	494	8.78 ± 0.03	10.11 ± 0.25	1.1
UGC 09618[a]	14:57:00.40	+24:36:44.0	0.0337	17.8 ± 1.3	545	8.58 ± 0.01	8.96 ± 0.54	1.0
SDSS J150539.56+574307.2	15:05:39.56	+57:43:07.3	0.1506[b]	< 8.74	⋯	8.71 ± 0.09	< 9.98	0.6
VV 705	15:18:06.34	+42:44:36.6	0.0405	44.3 ± 4.8	176	8.64 ± 0.01	9.52 ± 0.19	1.5
NGC 5992	15:44:21.51	+41:05:10.9	0.0320	17.0 ± 3.0	175	8.26 ± 0.05	8.89 ± 0.25	1.3
NGC 6090	16:11:40.70	+52:27:24.0	0.0295	71.9 ± 4.5	118	8.66 ± 0.02	9.48 ± 0.45	2.0
SDSS J163452.36+462452.5	16:34:52.36	+46:24:52.5	0.1908[b]	< 15.1	⋯	9.24 ± 0.06	< 10.43	0.8
2MASX J16491420+3425096	16:49:14.20	+34:25:09.7	0.1125	14.3 ± 2.5	678	9.12 ± 0.06	9.92 ± 0.25	0.7
CGCG 367-020	16:52:36.82	+81:00:16.6	0.0472	14.1 ± 3.2	160	8.69 ± 0.04	9.19 ± 0.26	1.7
NGC 6286	16:58:31.38	+58:56:10.5	0.0189	104.3 ± 18.6	560	8.09 ± 0.01	9.20 ± 0.42	3.4
2MASX J17034196+5813443	17:03:41.94	+58:13:44.7	0.1061[b]	< 12.6	⋯	8.84 ± 0.05	< 9.83	0.8
IRAS 17132+5313	17:14:20.00	+53:10:30.0	0.0513	23.4 ± 5.8	465	8.88 ± 0.03	9.45 ± 0.78	1.4
NGC 6670A	18:33:37.72	+59:53:22.8	0.0291	42.0 ± 2.4	149	8.40 ± 0.05	9.21 ± 0.24	1.1
NGC 6786	19:10:53.91	+73:24:36.6	0.0252	47.6 ± 3.5	172	8.25 ± 0.01	9.13 ± 0.21	1.2
NVSS J211129+582307	21:11:29.28	+58:23:07.9	0.0393	21.7 ± 4.0	255	8.17 ± 0.05	9.16 ± 0.25	1.4
3C 445	22:23:49.53	−02:06:12.9	0.0559[b]	< 12.0	⋯	< 8.26	< 9.24	0.6
NGC 7469	23:03:15.62	+08:52:26.3	0.0164	230.0 ± 4.0	208	8.29 ± 0.02	9.44 ± 0.02	1.2
Arp 295B	23:42:00.85	−03:36:54.6	0.0231	55.3 ± 10.7	411	8.29 ± 0.04	9.13 ± 0.25	1.9
2MASX J23460571+5313564	23:46:05.58	+53:14:00.6	0.0340	34.9 ± 3.7	186	8.26 ± 0.04	9.27 ± 0.24	1.2

Notes. Column (1): name of the source. Columns (2)–(3): coordinate of the source, defined as the KVN pointing coordinate. Column (4): redshift measured from the shift of CO(1–0) line, accounting for the velocity offset. Column (5): velocity-integrated flux within the integral interval (gray regions in Figure 3). Column (6): FWHM measured using single Gaussian fit or line width in the horn-shaped profile. Column (7): log $L_{3.3}$ compiled from literature. Column (8): log $L'_{CO(1-0)}$ calculated from the KVN observations. Column (9): rms in the T_A^* in the KVN observations.
[a] Merger/interacting source for which pointing coordinates for 3.3 μm observation and KVN observation are different.
[b] For sources with CO nondetection, redshift values are from the literature that contain $L_{3.3}$ values.

derived from the CO emission line, log $L_{3.3}$, log $L'_{CO(1-0)}$, and the rms noise are listed in Table 1. Note that the coordinates given in Table 1 are coordinates of the KVN pointings, which can be slightly offset from that of 3.3 μm PAH pointings especially in sources that are members of an interacting/merging system (see table notes). For six sources without CO detections, the 3σ flux upper limits are estimated assuming a line width of 300 km s^{-1}.

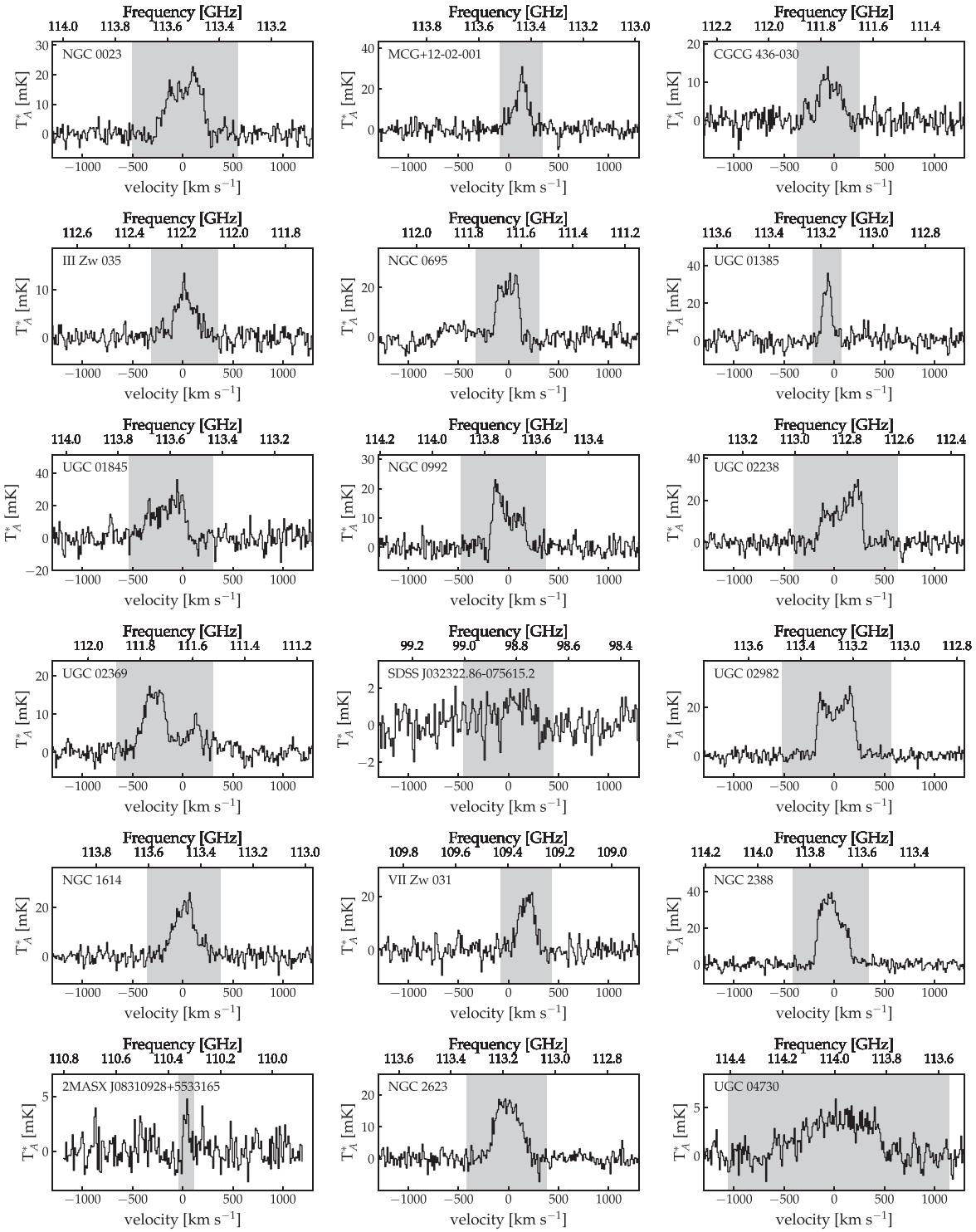

Figure 3. CO(1–0) spectra of 50 3.3 μm PAH-selected objects obtained from the KVN SD observations. All spectra are smoothed to a velocity resolution of $\sim$10 km s^{-1}. The gray shaded regions indicate the range of velocities used to compute the velocity-integrated flux density (equivalent to 3 times line width).

2.4. CO from Literature

We compiled the existing CO emission line measurements (from either SD or interferometry observations) for 3.3 μm PAH-selected sources from numerous literature (Table 2, J. S. Young et al. 1995; F. P. Israel et al. 2015; K. Morokuma-Matsui et al. 2015; S. M. Consiglio et al. 2016; N. Lu et al. 2017; T. Yamashita et al. 2017; I. Cortzen et al. 2019; R. Herrero-Illana et al. 2019; J. Shangguan et al. 2020; T. Kawamuro et al. 2021; E. Bellocchi et al. 2022; I. Lamperti et al. 2022; I. Montoya Arroyave et al. 2023). Many sources were targeted by more than one observing program; thus, we have at most five CO measurements from the literature for a single source. In the case of the interferometric CO observations that provide spatially resolved CO emission, we utilized the sum of the flux densities from individual components to account for the integrated value from the entire galaxy. For higher CO

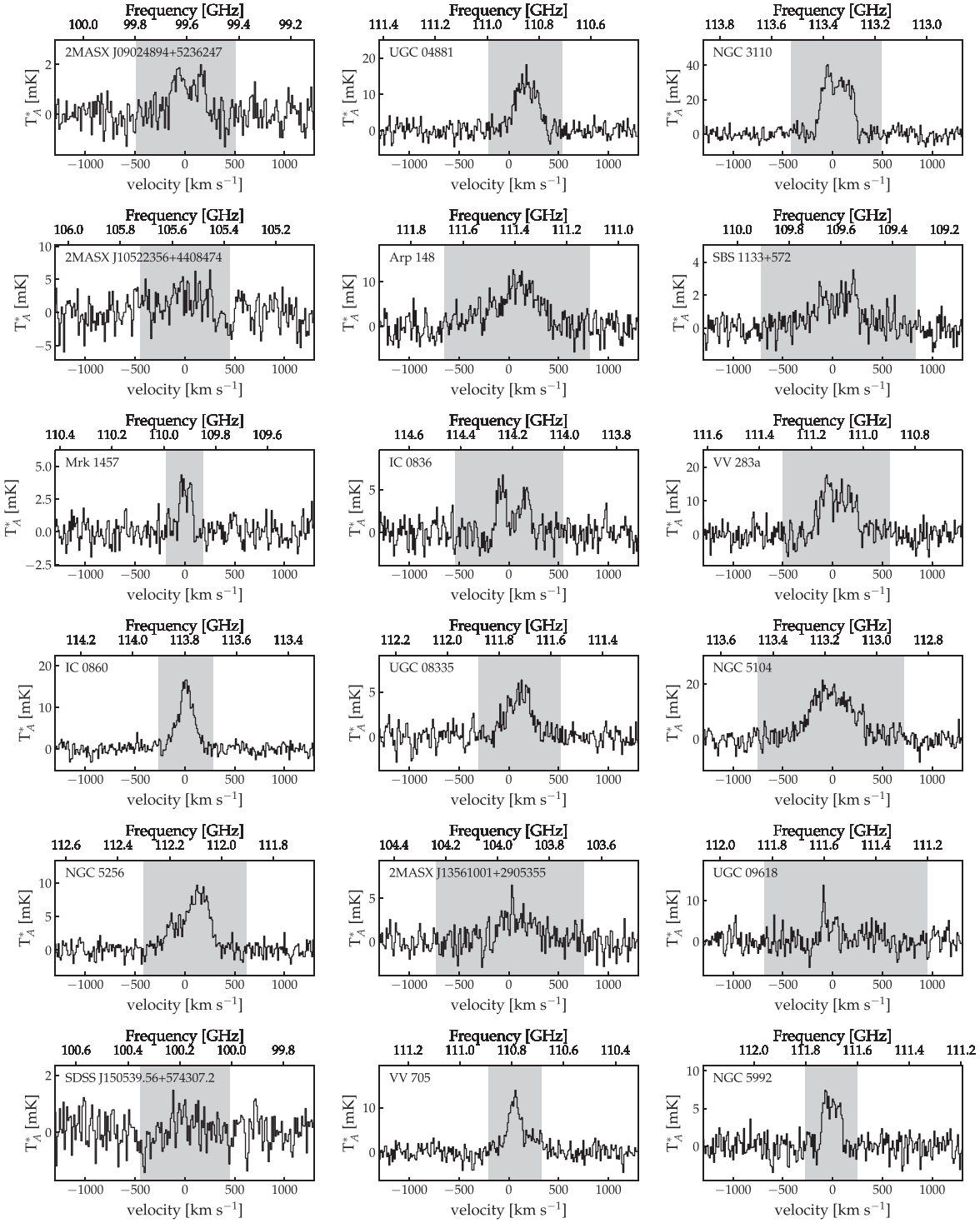

Figure 3. (Continued.)

transitions (e.g., $J > 1$ with $J-(J-1)$ transition), we converted the observed values to those for (1–0) transition using the line ratios measured for submillimeter galaxies (e.g., $r_{21/10} = 0.84 \pm 0.13$; M. S. Bothwell et al. 2013) considering the large SFR and IR luminosity of these galaxies. Note, however, since the ratios between different CO transition lines heavily depend on the physical conditions of the interstellar gas and the processes related to the star formation, the scatter in the line ratios is highly significant (e.g., $r_{21/10}$ ranging from 0.33 to 1.47) for LIRGs. Therefore, caution is needed when including high-J CO transitions in the construction of the PAH–CO calibration formula.

In the following analysis, if multiple CO measurements (from multiple literature) are available for one source, we adopt the values in the following order of preference: CO(1–0) SD (63 sources), CO(1–0) array (9 sources), CO(2−1) SD (4 sources), CO(2−1) array (7 sources), and high-J CO transitions (18 sources). Among these, 26 sources were included as targets for KVN observations (22 sources have CO(1–0) SD observations from literature). Figure 4 displays the comparison

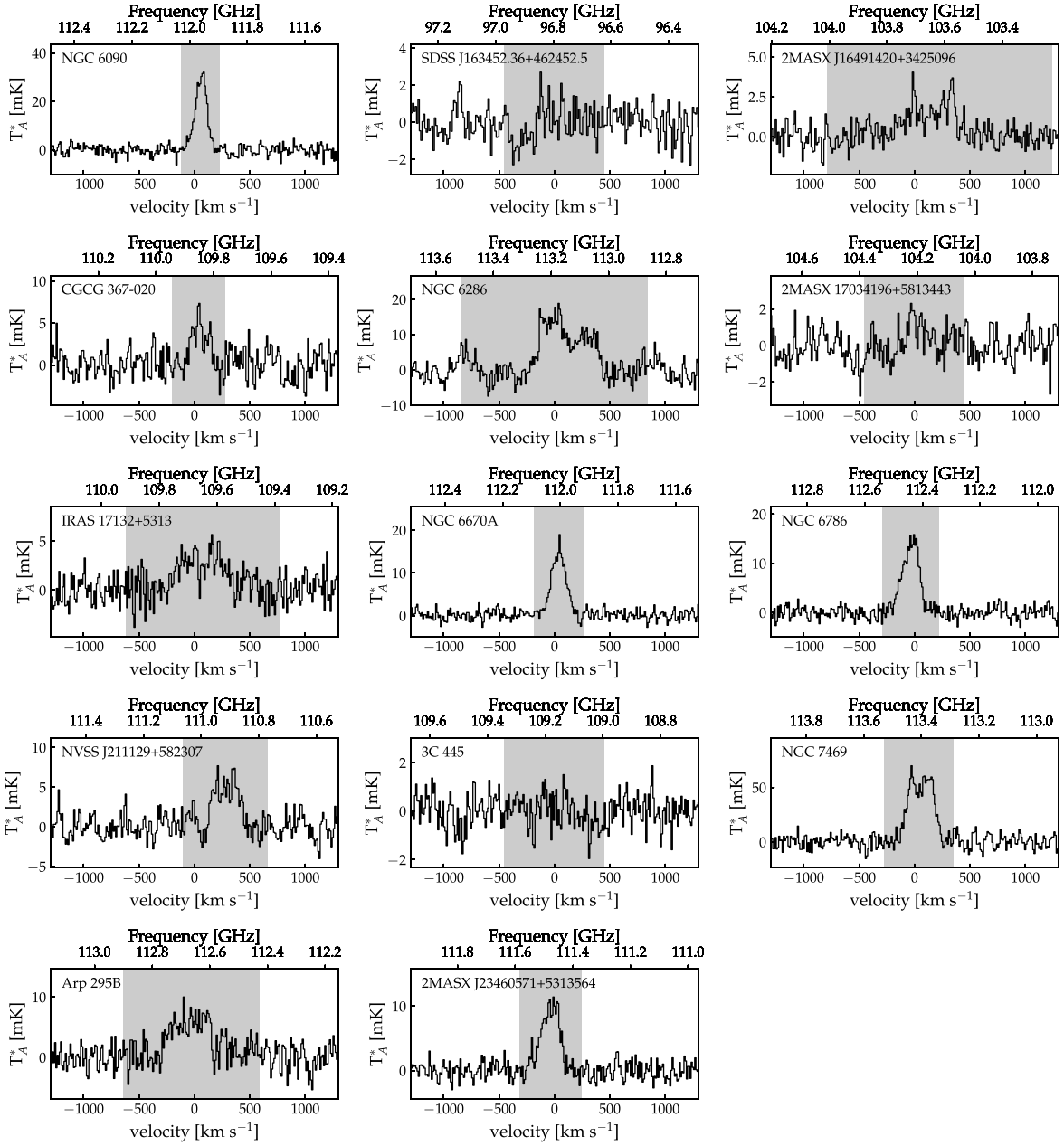

Figure 3. (Continued.)

between the CO(1–0) line luminosities from different observations. Among 63 sources with CO(1–0) SD observations, 48 sources have multiple CO observations including the other CO(1–0) SD, CO(1–0) array, CO(2−1) SD, CO(2−1) array, and high-J transition CO observations (top panel of Figure 4). Using $\log L'_{\mathrm{CO}(1-0)}$ value from one of the CO(1–0) SD observations (the value from the smallest telescope) as a reference value (i.e., $\log L'_{\mathrm{CO}(1-0),\,\mathrm{ref}}$), the mean difference ($\Delta \log L'_{\mathrm{CO}(1-0)} = \log L'_{\mathrm{CO}(1-0)} - \log L'_{\mathrm{CO}(1-0),\,\mathrm{ref}}$) among CO(1–0) SD observations is -0.022 ± 0.285 dex. Including different transitions and observation types (SD or array), the difference is -0.054 ± 0.362 dex. The intrinsic scatter in the $\log L'_{\mathrm{CO}(1-0)}$ values is relatively large (i.e., >0.3 dex). Note that the inclusion of large sources (i.e., objects with an optical diameter larger than 100″) tends to increase the scatter. However, the systematic offset between the values from different observations does not change significantly by including such large sources, as well as sources that are located within the interacting/merging system.

About half (26) of the KVN targets have CO measurements from literature (bottom panel of Figure 4). For these, the difference $\Delta \log L'_{\mathrm{CO}(1-0)}$ is 0.226 ± 0.239 dex, indicating that CO luminosities measured from KVN SD observations are slightly lower compared to the values measured by other observations (e.g., FCRAO; J. S. Young et al. 1995). One of the reasons could be a difference in the beam size between J. S. Young et al. (1995; 45″) and our work (30″) at ∼115 GHz; with the exclusion of J. S. Young et al. (1995) sample, $\Delta \log L'_{\mathrm{CO}(1-0)}$ for the KVN targets is 0.165 ± 0.230. These differences in $\log L'_{\mathrm{CO}(1-0)}$ were added to the uncertainties in CO luminosity. For KVN sources and literature sources with a single CO measurement, intrinsic scatters (i.e., 0.239 and

Table 2
Literature CO Observations

Literature	CO Line	$N_{3.3}$[a]	Telescope	Target Description
J. S. Young et al. (1995)	(1–0)	22	FCRAO (14 m, SD)	Nearby galaxies
K. Morokuma-Matsui et al. (2015)	(1–0)	2	Nobeyama (45 m, SD)	Normal star-forming galaxies ($0.1 < z < 0.2$)
T. Yamashita et al. (2017)	(1–0)	29	Nobeyama (45 m, SD)	LIRGs and ULIRGs
I. Cortzen et al. (2019)	(1–0)	6	IRAM (30 m, SD)	Star-forming galaxies ($0.03 < z < 0.28$)
R. Herrero-Illana et al. (2019)	(1–0)	23	IRAM (30 m, SD)	LIRGs and ULIRGs
I. Montoya Arroyave et al. (2023)	(1–0)	10	ALMA	Local (U)LIRGs
F. P. Israel et al. (2015)	(2−1)	13	JCMT (15 m, SD)	(U)LIRGs and starburst galaxies
J. Shangguan et al. (2020)	(2−1)	1	ALMA	Palomar-Green luminous quasars
T. Kawamuro et al. (2021)	(2−1)	3	ALMA	Hard X-ray selected AGN
I. Lamperti et al. (2022)	(2−1)	13	ALMA	Nearby ULIRG
E. Bellocchi et al. (2022)	(2−1)	1	ALMA	Local ($z < 0.02$) LIRGs
I. Montoya Arroyave et al. (2023)	(2−1)	2	APEX (12 m, SD)	Local (U)LIRGs
F. P. Israel et al. (2015)	(4−3), (7−6)	16	Herschel	(U)LIRGs and starburst galaxies
N. Lu et al. (2017)	(4−3), (5−4), (6−5), (7−6)	59	Herschel	Local LIRGs

Notes. Atacama Large Millimeter/submillimeter Array (ALMA). James Clerk Maxwell Telescope (JCMT).
[a] Number of galaxies where 3.3 μm flux, not upper limit, is available.

0.362) were added to uncertainties. Considering the relatively large systematic offset of the KVN $L'_{\rm CO}$ values to that from previous literature, in the following section, we derived $\log L_{3.3}-\log L'_{\rm CO(1-0)}$ relationships based on the KVN observations and literature compilation separately, in addition to using the entire combined sample.

3. Results and Discussion

3.1. $L_{3.3}$ versus $L'_{CO(1-0)}$ Correlation

We show the correlation between the 3.3 μm PAH luminosity and CO(1–0) luminosity in Figure 5, using sources with our KVN observations as well as sources from the literature. The linear fit describing scaling relations between different luminosities is obtained in the logarithmic space, with a form of $\log y = \alpha \times \log x + \beta$. The parameters, α and β, are summarized in Table 3. The parameters are estimated by exploiting a Bayesian approach described in B. C. Kelly (2007), which derives a posterior distribution of the linear regression coefficients through a Markov Chain Monte Carlo algorithm using a varying set of independent and dependent variables using their errors (uncertainties) as the dispersion of the distributions. The PYTHON implementation of the B. C. Kelly (2007) method, i.e., `LinMix`, allows the handling of nondetection (i.e., upper limits) by censoring specific data points. We present the fitting results from different subsamples in Table 3 as well, e.g., including CO nondetections (in the case of the KVN observations) and including 3.3 μm upper limits (in the case of the literature compilation).

Using 49 KVN sources (3.3 μm flux density available, including 5 sources with CO nondetection), the linear slope between $\log L_{3.3}$ and $\log L'_{\rm CO(1-0)}$ is slightly subunity (0.85 ± 0.12). Excluding CO nondetections, the slope is 0.97 ± 0.14, which is in line with the result of I. Cortzen et al. (2019) stating that the $L_{\rm PAH}/L'_{\rm CO}$ ratio is almost constant for star-forming galaxies in the case of 6.2 and 7.7 μm PAHs (Figure 5, left panel). The mean $\log (L_{3.3}/L'_{\rm CO(1-0)})$ value for 44 KVN sources is -0.91 [$L_\odot/$(K km s^{-1} pc^2)], with a standard deviation of 0.28. A similar relation is found from the linear fit for literature CO values; the slope is 1.09 ± 0.11 when sources with 3.3 μm upper limits are not considered. As is discussed in Sections 2.1 and 2.4, different treatment in dust attenuation

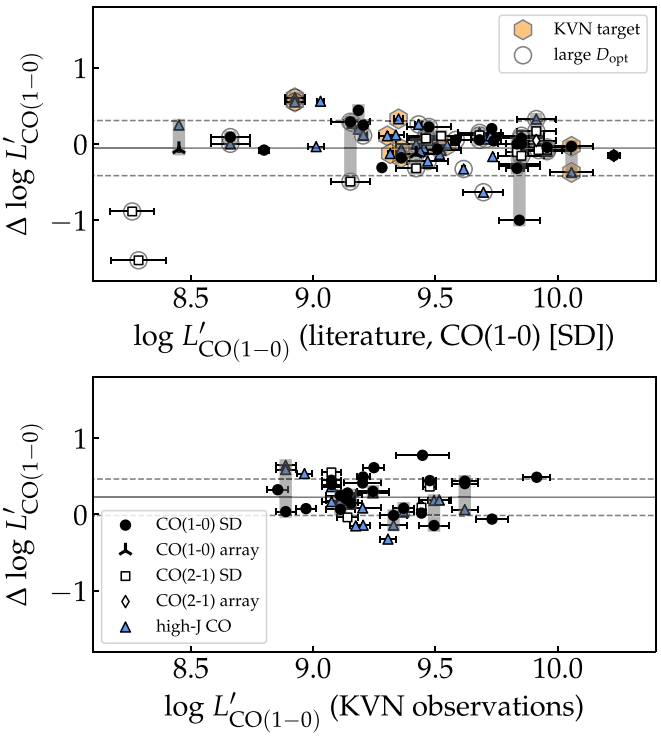

Figure 4. (Top) Comparison between the CO luminosities from different literature. Different CO transitions and observation types are plotted as different symbols (see legend in bottom panel). KVN targets and large sources are marked. Vertically connected points (with thick gray lines) indicate one identical source. Horizontal solid and dashed lines indicate mean difference and standard deviation (-0.054 ± 0.362). (Bottom) Difference of $\log L'_{\rm CO(1-0)}$ between our KVN observations and other literature. Again, the mean difference and standard deviation (0.226 ± 0.239) are indicated as horizontal lines.

correction and different CO observation strategies may affect the derived correlation between $L_{3.3}$ and $L'_{\rm CO}$ using the heterogeneous sample. Considering these, we fit the linear relation between $\log L_{3.3}$ and $\log L'_{\rm CO(1-0)}$ using a subsample of 49 sources from T. S. Y. Lai et al. (2020) that have CO(1–0) SD measurements. For this subsample, the slope is 1.01 ± 0.12, consistent with the result from the entire literature sample and KVN sample with the exclusion of sources with upper limits (either in CO or 3.3 μm).

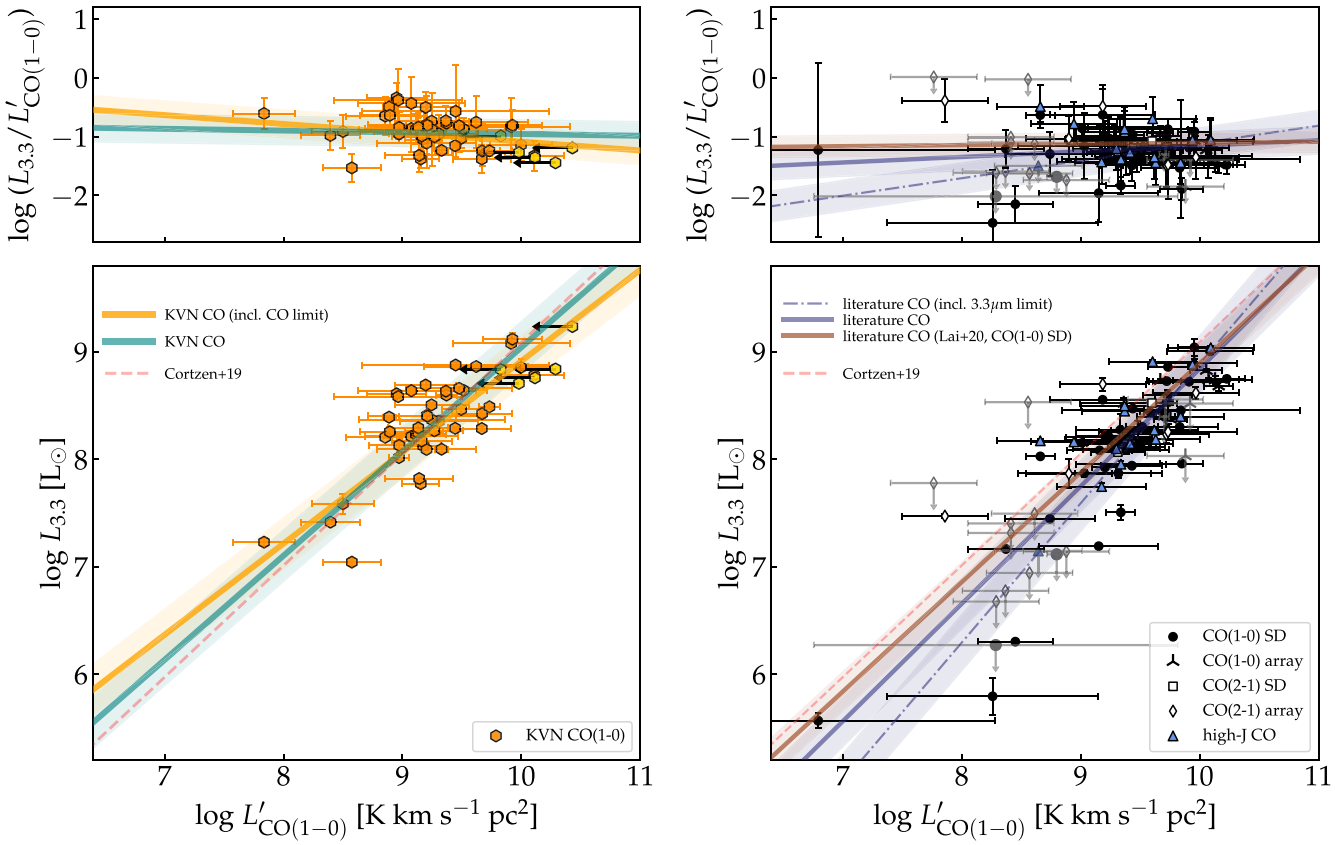

Figure 5. Correlation between 3.3 μm PAH luminosity and CO (1–0) luminosity constructed using KVN observations (left) and literature data (right, excluding KVN targets). New KVN observations of 49 sources selected at 3.3 μm (excluded one source with 3.3 μm upper limit) are plotted as orange-colored hexagons (44), while five yellow hexagons with leftward arrows represent sources for which the CO line was not detected. Different symbols represent sources with literature-derived log $L'_{\rm CO}$ values: CO (1–0) single dish, CO (1–0) interferometer array, CO (2−1) single dish, CO (2–1) interferometer array, and higher-J transitions. Nondetections (i.e., upper limits) are plotted as gray colors. Different solid lines (and the dashed–dotted line) show the best-fit linear correlations between log $L_{3.3}$ and log $L'_{\rm CO(1-0)}$ for different subsamples of sources. Shaded regions indicate the intrinsic scatter of the linear fits. Dashed lines in the lower panels denote the 7.7 μm PAH–CO relation suggested by I. Cortzen et al. (2019), vertically shifted by the average ratio between 3.3 and 7.7 μm PAH emissions (T. S. Y. Lai et al. 2020).

Table 3
Linear Scaling Relations between the 3.3 μm PAH, IR, and CO(1–0) Luminosities

x	y	α	β	σ^2	Sample	$N_{\rm source}$
$L_{3.3}$ [$L_\odot$]	$L_{\rm IR}$ [$L_\odot$]	0.80 ± 0.04	−0.85 ± 0.51	0.132	all	180
$L_{3.3}$ [$L_\odot$]	$L_{\rm IR}$ [$L_\odot$]	0.78 ± 0.04	−0.54 ± 0.50	0.102	detection only	150
$L_{3.3}$ [$L_\odot$]	$L_{\rm IR}$ [$L_\odot$]	0.75 ± 0.05	−0.24 ± 0.54	0.081	non-AGN	113
$L'_{\rm CO(1-0)}$ [K km s^{-1} pc^2]	$L_{3.3}$ [$L_\odot$]	0.85 ± 0.12	0.42 ± 1.13	0.056	KVN observations (all)	49
$L'_{\rm CO(1-0)}$ [K km s^{-1} pc^2]	$L_{3.3}$ [$L_\odot$]	0.97 ± 0.14	−0.66 ± 1.30	0.057	KVN observations (detection only)	44
$L'_{\rm CO(1-0)}$ [K km s^{-1} pc^2]	$L_{3.3}$ [$L_\odot$]	1.29 ± 0.11	−4.04 ± 1.08	0.068	literature (all)	86
$L'_{\rm CO(1-0)}$ [K km s^{-1} pc^2]	$L_{3.3}$ [$L_\odot$]	1.09 ± 0.11	−2.11 ± 1.00	0.054	literature (detection only)	70
$L'_{\rm CO(1-0)}$ [K km s^{-1} pc^2]	$L_{3.3}$ [$L_\odot$]	1.01 ± 0.12	−1.26 ± 1.13	0.033	literature (subsample[a])	49
$L'_{\rm CO(1-0)}$ [K km s^{-1} pc^2]	$L_{3.3}$ [$L_\odot$]	1.10 ± 0.08	−2.08 ± 0.75	0.063	KVN+literature (all)	135
$L'_{\rm CO(1-0)}$ [K km s^{-1} pc^2]	$L_{3.3}$ [$L_\odot$]	1.00 ± 0.07	−1.10 ± 0.70	0.055	KVN+literature (detection only)	114
$L'_{\rm CO(1-0)}$ [K km s^{-1} pc^2]	$L_{3.3}$ [$L_\odot$]	1.56 ± 0.84	−6.39 ± 7.85	0.131	KVN observations (AGN)	9
$L'_{\rm CO(1-0)}$ [K km s^{-1} pc^2]	$L_{3.3}$ [$L_\odot$]	0.90 ± 0.15	0.07 ± 1.34	0.051	KVN observations (non-AGN)	35
$L'_{\rm CO(1-0)}$ [K km s^{-1} pc^2]	$L_{3.3}$ [$L_\odot$]	1.37 ± 0.20	−4.82 ± 1.87	0.069	KVN+literature (AGN)	25
$L'_{\rm CO(1-0)}$ [K km s^{-1} pc^2]	$L_{3.3}$ [$L_\odot$]	0.87 ± 0.08	0.18 ± 0.72	0.048	KVN+literature (non-AGN)	89

Notes. Linear scaling relations are found in the form of $\log y = \alpha \times \log x + \beta$.
[a] Sources from T. S. Y. Lai et al. (2020) for which CO(1–0) SD observations are available.

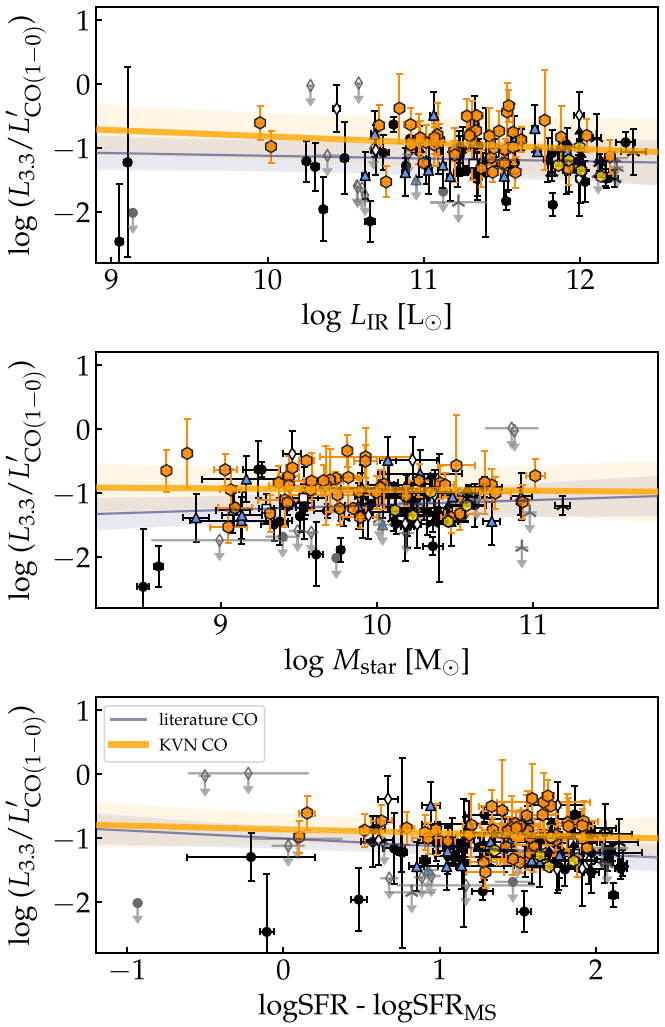

Figure 6. The ratio between 3.3 μm PAH and CO luminosities in units of [$L_\odot$/(K km s^{-1} pc^2)] as a function of total IR luminosity (top), stellar mass (middle), and offset from the star-forming galaxy main sequence (bottom). Symbols are as defined in Figure 5. Overplotted solid lines indicate linear correlations constructed using CO luminosity data points compiled from the literature and obtained from KVN observations.

If KVN and literature samples are combined (114 sources excluding upper limits), the relation between log $L_{3.3}/L_\odot$ and log $L'_{CO(1-0)}$/(K km s^{-1} pc^2) is described as follows:

$$\log L_{3.3} = (1.00 \pm 0.07) \times \log L'_{CO(1-0)} + (-1.10 \pm 0.70). \quad (3)$$

The slope is close to unity (1.00 ± 0.07), clearly suggesting the possibility that PAH emission can be used to estimate the amount of molecular gas in galaxies. The constant conversion factor between $L_{3.3}$ and $L'_{CO(1-0)}$ is

$$\log (L_{3.3}/L'_{CO(1-0)}) = -1.09 \pm 0.36, \quad (4)$$

in units of [$L_\odot$/(K km s^{-1} pc^2)].

Note that the trend in log $L_{3.3}$–log $L'_{CO(1-0)}$ space remains unchanged if the large sources (optical diameter larger than 100″, marked in the top panel of Figure 4) and/or interacting/merging galaxies are excluded. To explore factors responsible for the scatter in the observed $L_{3.3}$–L'_{CO} correlation, we display the $L_{3.3}/L'_{CO}$ ratios as a function of IR luminosity, stellar mass, and star formation activity (Figure 6). Star formation activity is

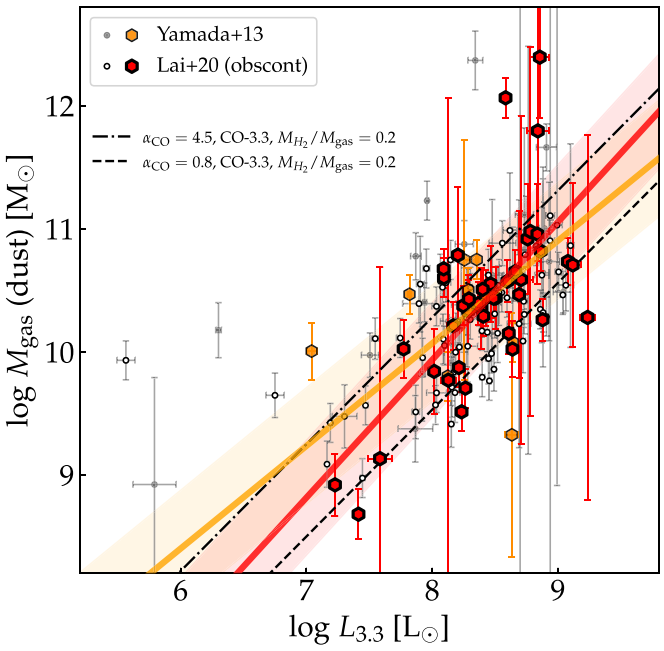

Figure 7. Correlation between the gas mass estimated from dust mass ($M_{gas} \equiv M_{HI} + M_{H_2}$) and 3.3 μm PAH luminosity. Colored symbols represent KVN targets (including CO nondetections), while the white/gray symbols are sources from the literature. Dashed–dotted and dashed lines represent the M_{H_2} vs. CO luminosity relationships assuming $M_{H_2}/M_{gas} = 0.2$ in addition to $\alpha_{CO} = 4.5$ and 0.8, respectively, of which CO luminosity is converted from the 3.3 μm PAH luminosity using the derived correlation in Figure 5 (teal line using 44 KVN sources; Table 3). Overplotted solid lines are the best-fit linear relationships between log M_{gas} and log $L_{3.3}$ using all 49 KVN sources (orange) and 41 KVN sources from T. S. Y. Lai et al. (2020; red).

defined as the offset from the star-forming main sequence, where SFR$_{MS}$ is a function of stellar mass and redshift (J. S. Speagle et al. 2014). In all three panels, the Spearman coefficients are too low (with p-values exceeding 0.1); thus, it cannot be concluded that the scatter in 3.3 μm PAH–CO ratios is driven by the different physical properties of galaxies.

3.2. Molecular Gas Mass and $L_{3.3}$

The molecular gas mass of a galaxy can be estimated from the observed CO luminosity by applying a CO–H_2 conversion factor (i.e., $M(H_2) \equiv \alpha_{CO} \times L'_{CO}$). The α_{CO} factor exhibits a large variation for different galaxies (e.g., A. K. Leroy et al. 2011; P. P. Papadopoulos et al. 2012), and is suggested to be governed by interstellar medium characteristics in star-forming regions such as the metallicity, gas temperature, velocity dispersion, and surface density (D. Narayanan et al. 2012; A. D. Bolatto et al. 2013). The α_{CO} factor for normal main-sequence star-forming galaxies is similar to the average value in Milky Way disks (P. M. Solomon et al. 1987), i.e., $\langle\alpha_{CO}\rangle \sim 4.4\,M_\odot/(\mathrm{K\,km\,s^{-1}\,pc^2})$, while the α_{CO} factor for extreme starburst environments is lower (∼0.8; D. Downes & P. M. Solomon 1998) when measured for local ULIRGs and high-redshift starburst galaxies, due to the increased gas temperature and velocity dispersion. In a low-metallicity environment with less metal shielding, however, α_{CO} is reported to increase (D. Narayanan et al. 2012), as CO molecules are destroyed through photodissociation. To overcome the issues related to this α_{CO} uncertainty, alternative methods, such as using dust emission and scaling relations to estimate gas mass, are being introduced and utilized, especially

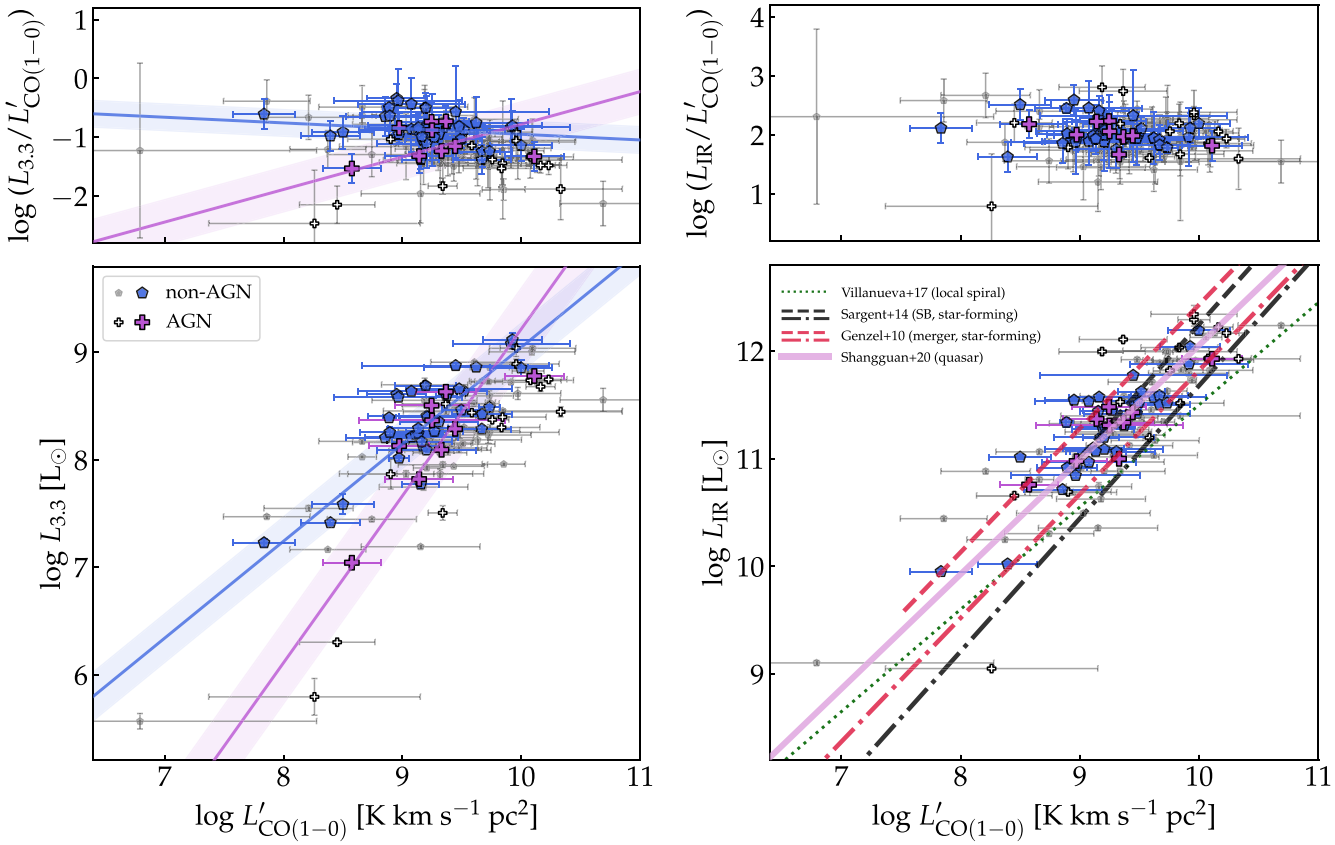

Figure 8. (Left) Correlation between 3.3 μm PAH luminosity and CO luminosity for AGN (crosses) and non-AGN sources (pentagons). Colored symbols (purple crosses, blue pentagons) represent KVN sources, while the white/gray symbols represent sources from the literature. Best-fit linear relation between log $L_{3.3}$ and log $L'_{CO(1-0)}$ are constructed using the KVN sources, excluding nondetections. (Right) Correlation between total IR luminosity and CO luminosity for AGN and non-AGN. Overplotted lines represent the log L_{IR}–log $L'_{CO(1-0)}$ calibrations from different literature; green dotted line for local spiral galaxies (V. Villanueva et al. 2017), dashed–dotted lines for star-forming galaxies (black from M. T. Sargent et al. 2014; and crimson from R. Genzel et al. 2010, respectively), dashed lines for starbursts (M. T. Sargent et al. 2014) and luminous mergers (R. Genzel et al. 2010), and pink solid line for quasar hosts (J. Shangguan et al. 2020). For starbursts, the lines are drawn in the IR luminosity range that cover the sample galaxies used in deriving the calibrations.

in surveys with (rest-frame) FIR photometric information (e.g., S. Berta et al. 2016; C. Bertemes et al. 2018).

For 3.3 μm selected sources with KVN CO(1–0) observations, we estimated their gas mass (M_{gas}) based on the dust mass (M_{dust}) and gas-to-dust mass ratio ($\delta_{GDR} \equiv M_{gas}/M_{dust}$). The dust mass of the sources was estimated by fitting IR SED to dust emission models (B. T. Draine et al. 2014) within the SED fitting code CIGALE (M. Boquien et al. 2019) as described in Section 2.1, assuming that the dust emission is proportional to the dust mass illuminated by a power-law-shaped radiation field intensity. We used the metallicity-dependent gas-to-dust mass ratio (G. E. Magdis et al. 2012) by applying the (gas-phase) metallicity inferred through the fundamental mass–SFR–metallicity relation (F. Mannucci et al. 2010) along with the SED fitting-derived stellar mass and SFR for these sources. Note that the uncertainty in the derived gas mass is generally large, reflecting photometric uncertainties in the FIR wavelengths, uncertainties in the derived stellar mass and SFR used to estimate metallicity, and uncertainties inherent in the empirical relations as well.

Figure 7 shows the correlation between the gas mass estimated from the dust emission and 3.3 μm luminosity. The gas mass described here is the sum of the molecular hydrogen and atomic hydrogen, and the mass ratio M_{H_2}/M_{HI} varies across different star-forming environments, with a connection to the gas surface density. This complicates the interpretation of the M_{gas}–$L_{3.3}$ correlation. Despite a large scatter, the Spearman rank coefficient between log $M_{gas}/M_\odot$ and log $L_{3.3}/L_\odot$ is statistically significant (with a p-value less than 10^{-4}), and the correlation is approximated by the following linear relation with a scatter of $\sigma \sim 0.46$:

$$\log M_{gas} = (0.83 \pm 0.19) \times \log L_{3.3} + (3.40 \pm 1.63). \quad (5)$$

If the sample is limited to 41 KVN sources with 3.3 μm measurements from T. S. Y. Lai et al. (2020), the correlation is slightly different, and described as follows:

$$\log M_{gas} = (1.12 \pm 0.23) \times \log L_{3.3} + (0.98 \pm 1.92). \quad (6)$$

The 1σ uncertainty regions suggested by these correlations are comparable to the space covered by $M_{H_2} = \alpha_{CO} L'_{CO}$ correlation with $\alpha_{CO} = 0.8$–4.5, assuming a mass ratio M_{H_2}/M_{gas} of 0.2 (for late-type spirals; J. S. Young & N. Z. Scoville 1991). The range of the assumed α_{CO} values suggests that the derived log M_{gas}–log $L_{3.3}$ correlation is applicable to the wide range of star-forming galaxies, from normal disk galaxies to extreme starbursts.

Although our KVN targets did not include sources with log $(L_{3.3}/L_\odot) < 7$, Figure 7 shows that there exist several sources that are expected to have significant amounts of gas despite low PAH luminosity, e.g., low-metallicity galaxy II Zw 40 with log $(L_{3.3}/L_\odot) < 6$. The presence of these increases scatters in the derived linear relation between

log $M_{\rm gas}$ and log $L_{3.3}$, and needs to be explored further with the increased number of sources for which $L_{3.3}$ is measured at a low luminosity range.

3.3. $L_{3.3}$, L_{IR}, and L'_{CO} for AGN

As a star formation tracer, PAH emission has been used to estimate the SFR in AGN host galaxies (D. Lutz et al. 2008; J. H. Kim et al. 2019) as well as in star-forming galaxies. Since the radiation field characteristics in the vicinity of an AGN (e.g., close to the central region of an AGN host galaxy) and in the average star-forming disk could differ, the PAH-SFR calibration for AGN might be different from that generally used for star-forming galaxies (E. Peeters et al. 2004). PAH molecule destruction in the strong radiation field (G. M. Voit 1992; V. Desai et al. 2007) may lead to a weak PAH emission in the spectra of AGN host galaxies.

In Figure 8, we present $L_{3.3}$–$L'_{\rm CO}$ correlations and $L_{\rm IR}$–$L'_{\rm CO}$ correlations for AGN and non-AGN (i.e., star-forming galaxies) separately (listed in Table 3). The two populations are not distinguished in the log $L_{\rm IR}$ versus log $L'_{\rm CO}$ space (right panel). However, in the log $L_{3.3}$ versus log $L'_{\rm CO}$ diagram (left panel), the two populations are discriminated against; the slope in the log $L_{3.3}$–log $L'_{\rm CO}$ relation is steeper in the case of the AGN (1.56 ± 0.84) than in the case of non-AGN (0.90 ± 0.15). This implies that, in AGN with low CO luminosity, 3.3 μm PAH emission is weaker than in star-forming galaxies.

Previous works have suggested the scatter in log $L_{\rm IR}$–log $L'_{\rm CO}$ can be explained as either a separate log $(L_{\rm IR}/L'_{\rm CO(1-0)})$ ratio for starburst and normal star-forming galaxies (with the latter being lower than the former) or a single relation $L_{\rm IR} \propto {L'_{\rm CO}}^{k}$ where the slope k is larger than unity (M. T. Sargent et al. 2014). In the right panel of Figure 8, the KVN sources are located in between the log $L_{\rm IR}$–log $L'_{\rm CO}$ trends of the star-forming and starburst galaxies (e.g., R. Genzel et al. 2010; M. T. Sargent et al. 2014), and are also consistent with that of the quasar host galaxies (J. Shangguan et al. 2020). Although the number of AGN in our KVN sample is very small (only nine, excluding nondetections), the fact that the AGN show a comparable slope in log $L_{\rm IR}$ versus log $L'_{\rm CO}$ space suggests that the global star formation efficiency in AGN host galaxies is not significantly enhanced (P. Santini et al. 2012) or suppressed compared to inactive star-forming galaxies.

However, it is still a matter of question whether 3.3 μm PAH emission can serve as a reliable tracer of SFR in AGN host galaxies, as in the case of the other PAH features at longer wavelengths. Further studies on the ratios between different PAH feature strengths (e.g., D. Rigopoulou et al. 2021) using the spatially resolved data (e.g., T. S. Y. Lai et al. 2023) and the increased sample size from upcoming NIR spectrophotometric surveys would be required to assess the viability of using 3.3 μm PAH as an SFR indicator.

4. Conclusion

Combining new CO(1–0) observations of 50 3.3 μm selected sources (including both star-forming galaxies and AGN) with an existing literature compilation of CO data, we have constructed a correlation between 3.3 μm PAH luminosity and CO luminosity. This correlation is applicable to estimating (molecular) gas mass and star formation efficiency in galaxies. Our sample galaxies cover an IR luminosity range of log $(L_{\rm IR}/L_{\odot}) = 10$–$12$. The sample size of galaxies for which both 3.3 μm and CO(1–0) observations are available has been increased by a factor of $\sim$1.6 by our CO observations.

In the log $L_{3.3}$–log $L'_{\rm CO}$ space, we establish a linear correlation between the two variables, using log $L'_{\rm CO}$ as the independent variable. The slope is close to unity, suggesting that it is possible to use a single value of $\langle \log (L_{3.3}/L'_{\rm CO}) \rangle = -1.09$ for $L_{3.3}$ in units of $L_{\odot}$ and $L'_{\rm CO}$ in units of K km s^{-1} pc^2, with a scatter of $\sim$0.36 (based on the entire sample including KVN and literature, excluding nondetections). The scatter in the $L_{3.3}/L'_{\rm CO}$ is not correlated with IR luminosity, stellar mass, and SFR excess. Based on the derived conversion formula between log $L_{3.3}$ and log $L'_{\rm CO}$, we suggest a scaling relation between the 3.3 μm luminosity and gas mass (total gas mass, defined as the sum of molecular and atomic mass), which overlaps with previous CO–H_2 conversion factors for starbursts to main-sequence star-forming galaxies. The global star formation efficiency, reflected in the $L_{\rm IR}/L'_{\rm CO}$, for AGN and non-AGN, is consistent with each other based on the KVN sources. However, it is suspected that AGN show different trends in the log $L_{3.3}$–log $L'_{\rm CO}$ space compared to non-AGN, which needs to be verified by further studies using the increased number of 3.3 μm selected sources. With the upcoming availability of all-sky spectrophotometric surveys covering wavelengths 1–5 μm, the potential of using 3.3 μm PAH emission in estimating the gas mass would be tested further, for which scaling relation can be applied to galaxies at various cosmic epochs.

Acknowledgments

The authors would like to thank the referee for providing helpful suggestions to improve the manuscript. The KVN is a facility operated by the Korea Astronomy and Space Science Institute (KASI). We are particularly grateful to Dr. Do-Heung Je and Dr. Do-Young Byun, who developed the KVN 86 GHz wideband receiver and operating system. This upgrade enabled KVN to observe the rest CO(1–0) frequency. This work was supported by the National Research Foundation of Korea (NRF) grant funded by the Korea government (MSIT; Nos. 2022R1A4A3031306, 2022R1A6A3A01085930, RS-2024-00349364, 2021R1C1C1013580).

Facilities: KVN, Akari (IRC and FIS), GALEX, Sloan, UKIRT, WISE, Herschel (SPIRE), IRAS.

Software: Astropy (Astropy Collaboration et al. 2013, 2018), CIGALE (S. Noll et al. 2009; M. Boquien et al. 2019), GILDAS/CLASS (Gildas Team 2013), `linmix` (B. C. Kelly 2007), matplotlib (J. D. Hunter 2007), NumPy (S. van der Walt et al. 2011).

ORCID iDs

Hyunjin Shim https://orcid.org/0000-0002-4179-2628
Junhyun Baek https://orcid.org/0000-0002-3744-6714
Dohyeong Kim https://orcid.org/0000-0002-6925-4821
Minjin Kim https://orcid.org/0000-0002-3560-0781
Hyunmi Song https://orcid.org/0000-0002-4362-4070
Gu Lim https://orcid.org/0000-0002-5760-8186

References

Alam, S., Albareti, F. D., Allende Prieto, C., et al. 2015, ApJS, 219, 12
Astropy Collaboration, Price-Whelan, A. M., Sipőcz, B. M., et al. 2018, AJ, 156, 123

Astropy Collaboration, Robitaille, T. P., Tollerud, E. J., et al. 2013, A&A, 558, A33
Behroozi, P. S., Wechsler, R. H., & Conroy, C. 2013, ApJL, 762, L31
Bellocchi, E., Pereira-Santaella, M., Colina, L., et al. 2022, A&A, 664, A60
Berta, S., Lutz, D., Genzel, R., Förster-Schreiber, N. M., & Tacconi, L. J. 2016, A&A, 587, A73
Bertemes, C., Wuyts, S., Lutz, D., et al. 2018, MNRAS, 478, 1442
Bianchi, L., Shiao, B., & Thilker, D. 2017, ApJS, 230, 24
Bolatto, A. D., Wolfire, M., & Leroy, A. K. 2013, ARA&A, 51, 207
Boquien, M., Burgarella, D., Roehlly, Y., et al. 2019, A&A, 622, A103
Bothwell, M. S., Smail, I., Chapman, S. C., et al. 2013, MNRAS, 429, 3047
Bouché, N., Dekel, A., Genzel, R., et al. 2010, ApJ, 718, 1001
Bruzual, G., & Charlot, S. 2003, MNRAS, 344, 1000
Chastenet, J., Sutter, J., Sandstrom, K., et al. 2023, ApJL, 944, L11
Chown, R., Leroy, A. K., Sandstrom, K., et al. 2025, ApJ, 983, 64
Consiglio, S. M., Turner, J. L., Beck, S., & Meier, D. S. 2016, ApJL, 833, L6
Cortzen, I., Garrett, J., Magdis, G., et al. 2019, MNRAS, 482, 1618
Daddi, E., Bournaud, F., Walter, F., et al. 2010, ApJ, 713, 686
Desai, V., Armus, L., Spoon, H. W. W., et al. 2007, ApJ, 669, 810
Doré, O., Werner, M. W., Ashby, M. L. N., et al. 2018, arXiv:1805.05489
Downes, D., & Solomon, P. M. 1998, ApJ, 507, 615
Draine, B. T., Aniano, G., Krause, O., et al. 2014, ApJ, 780, 172
Elbaz, D., Dickinson, M., Hwang, H. S., et al. 2011, A&A, 533, A119
Fritz, J., Franceschini, A., & Hatziminaoglou, E. 2006, MNRAS, 366, 767
García-Burillo, S., Usero, A., Alonso-Herrero, A., et al. 2012, A&A, 539, A8
Genzel, R., Tacconi, L. J., Gracia-Carpio, J., et al. 2010, MNRAS, 407, 2091
Gildas Team 2013, ILDAS: Grenoble Image and Line Data Analysis Software, Astrophysics Source Code Library, ascl:1305.010
Hernán-Caballero, A., Spoon, H. W. W., Lebouteiller, V., Rupke, D. S. N., & Barry, D. P. 2016, MNRAS, 455, 1796
Herrero-Illana, R., Privon, G. C., Evans, A. S., et al. 2019, A&A, 628, A71
Herschel Team, Schulz, B., Marton, G., et al. 2024, yCat, VIII/112
Hunter, J. D. 2007, CSE, 9, 90
Imanishi, M., Nakagawa, T., Ohyama, Y., et al. 2008, PASJ, 60, S489
Imanishi, M., Nakagawa, T., Shirahata, M., Ohyama, Y., & Onaka, T. 2010, ApJ, 721, 1233
Israel, F. P., Rosenberg, M. J. F., & van der Werf, P. 2015, A&A, 578, A95
Jarrett, T. H., Cohen, M., Masci, F., et al. 2011, ApJ, 735, 112
Kawamuro, T., Ricci, C., Izumi, T., et al. 2021, ApJS, 257, 64
Kelly, B. C. 2007, ApJ, 665, 1489
Kennicutt, R. C., Jr. 1998, ApJ, 498, 541
Kim, J. H., Im, M., Kim, D., et al. 2019, PASJ, 71, 25
Lai, T. S. Y., Armus, L., Bianchin, M., et al. 2023, ApJL, 957, L26
Lai, T. S. Y., Smith, J. D. T., Baba, S., Spoon, H. W. W., & Imanishi, M. 2020, ApJ, 905, 55
Lamperti, I., Pereira-Santaella, M., Perna, M., et al. 2022, A&A, 668, A45
Lawrence, A., Warren, S. J., Almaini, O., et al. 2007, MNRAS, 379, 1599
Lee, S.-S., Byun, D.-Y., Oh, C. S., et al. 2011, PASP, 123, 1398
Leroy, A. K., Bolatto, A., Gordon, K., et al. 2011, ApJ, 737, 12
Leroy, A. K., Bolatto, A. D., Sandstrom, K., et al. 2023, ApJL, 944, L10
Leroy, A. K., Walter, F., Brinks, E., et al. 2008, AJ, 136, 2782
Lilly, S. J., Carollo, C. M., Pipino, A., Renzini, A., & Peng, Y. 2013, ApJ, 772, 119
Lu, N., Zhao, Y., Díaz-Santos, T., et al. 2017, ApJS, 230, 1
Lutz, D., Sturm, E., Tacconi, L. J., et al. 2008, ApJ, 684, 853
Madau, P., & Dickinson, M. 2014, ARA&A, 52, 415
Magdis, G. E., Daddi, E., Béthermin, M., et al. 2012, ApJ, 760, 6
Mannucci, F., Cresci, G., Maiolino, R., Marconi, A., & Gnerucci, A. 2010, MNRAS, 408, 2115
Mateos, S., Alonso-Herrero, A., Carrera, F. J., et al. 2012, MNRAS, 426, 3271
Montoya Arroyave, I., Cicone, C., Makroleivaditi, E., et al. 2023, A&A, 673, A13
Morokuma-Matsui, K., Baba, J., Sorai, K., & Kuno, N. 2015, PASJ, 67, 36
Moshir, M., Kopman, G., & Conrow, T. A. O. 1992, in IRAS Faint Source Survey, Explanatory Supplement Version 2, ed. M. Moshir, G. Kopman, & T. Conrow (Pasadena, CA: California Institute of Technology)
Narayanan, D., Krumholz, M. R., Ostriker, E. C., & Hernquist, L. 2012, MNRAS, 421, 3127
Noll, S., Burgarella, D., Giovannoli, E., et al. 2009, A&A, 507, 1793
Ohyama, Y., Onaka, T., Matsuhara, H., et al. 2007, PASJ, 59, S411
Onaka, T., Matsuhara, H., Wada, T., et al. 2007, PASJ, 59, S401
Oyabu, S., Ishihara, D., Malkan, M., et al. 2011, A&A, 529, A122
Papadopoulos, P. P., van der Werf, P., Xilouris, E., Isaak, K. G., & Gao, Y. 2012, ApJ, 751, 10
Peeters, E., Spoon, H. W. W., & Tielens, A. G. G. M. 2004, ApJ, 613, 986
Pope, A., Chary, R.-R., Alexander, D. M., et al. 2008, ApJ, 675, 1171
Pope, A., Wagg, J., Frayer, D., et al. 2013, ApJ, 772, 92
Popesso, P., Concas, A., Cresci, G., et al. 2023, MNRAS, 519, 1526
Rémy-Ruyer, A., Madden, S. C., Galliano, F., et al. 2014, A&A, 563, A31
Rigopoulou, D., Barale, M., Clary, D. C., et al. 2021, MNRAS, 504, 5287
Saintonge, A., Kauffmann, G., Kramer, C., et al. 2011, MNRAS, 415, 32
Santini, P., Rosario, D. J., Shao, L., et al. 2012, A&A, 540, A109
Sargent, M. T., Daddi, E., Béthermin, M., et al. 2014, ApJ, 793, 19
Schmidt, M. 1959, ApJ, 129, 243
Scoville, N., Aussel, H., Sheth, K., et al. 2014, ApJ, 783, 84
Scoville, N., Sheth, K., Aussel, H., et al. 2016, ApJ, 820, 83
Shangguan, J., Ho, L. C., Bauer, F. E., Wang, R., & Treister, E. 2020, ApJS, 247, 15
Shim, H., Hwang, H. S., Jeong, W.-S., et al. 2023, AJ, 165, 31
Shipley, H. V., Papovich, C., Rieke, G. H., Brown, M. J. I., & Moustakas, J. 2016, ApJ, 818, 60
Skrutskie, M. F., Cutri, R. M., Stiening, R., et al. 2006, AJ, 131, 1163
Solomon, P. M., Downes, D., Radford, S. J. E., & Barrett, J. W. 1997, ApJ, 478, 144
Solomon, P. M., Rivolo, A. R., Barrett, J., & Yahil, A. 1987, ApJ, 319, 730
Solomon, P. M., & Vanden Bout, P. A. 2005, ARA&A, 43, 677
Speagle, J. S., Steinhardt, C. L., Capak, P. L., & Silverman, J. D. 2014, ApJS, 214, 15
Spoon, H. W. W., Hernán-Caballero, A., Rupke, D., et al. 2022, ApJS, 259, 37
Tacconi, L. J., Genzel, R., Neri, R., et al. 2010, Natur, 463, 781
Tremonti, C. A., Heckman, T. M., Kauffmann, G., et al. 2004, ApJ, 613, 898
van der Walt, S., Colbert, S. C., & Varoquaux, G. 2011, CSE, 13, 22
Villanueva, V., Ibar, E., Hughes, T. M., et al. 2017, MNRAS, 470, 3775
Voit, G. M. 1992, MNRAS, 258, 841
Wang, T.-W., Goto, T., Kim, S. J., et al. 2020, MNRAS, 499, 4068
Wright, E. L., Eisenhardt, P. R. M., Mainzer, A. K., et al. 2010, AJ, 140, 1868
Wuyts, S., Förster Schreiber, N. M., van der Wel, A., et al. 2011, ApJ, 742, 96
Yamada, R., Oyabu, S., Kaneda, H., et al. 2013, PASJ, 65, 103
Yamamura, I., Makiuti, S., Ikeda, N., et al. 2010, yCat, II/298
Yamashita, T., Komugi, S., Matsuhara, H., et al. 2017, ApJ, 844, 96
Young, J. S., & Scoville, N. Z. 1991, ARA&A, 29, 581
Young, J. S., Xie, S., Tacconi, L., et al. 1995, ApJS, 98, 219